CIRP Annals - Manufacturing Technology 72 (2023) 255–258

Contents lists available at ScienceDirect

CIRP Annals - Manufacturing Technology

journal homepage: https://www.editorialmanager.com/CIRP/default.aspx

An upset geometry sequence for determining the formability limits in bulk forming

Carlos M.A. Silva[a], Rui F.V. Sampaio[a], João P.M. Pragana[b], Ivo M.F. Bragança[a], Paulo A.F. Martins (1)[a,*]

[a] IDMEC, Instituto Superior Tecnico, Universidade de Lisboa, 1049-001 Lisbon, Portugal
[b] CIMOSM, Instituto Superior de Engenharia de Lisboa, Instituto Politécnico de Lisboa, 1959-007 Lisbon, Portugal

ARTICLE INFO

Article history:
Available online 2 May 2023

Keywords:
Metal forming
Fracture analysis
Formability limits

ABSTRACT

This paper presents an upset geometry sequence capable of providing strain loading paths from uniaxial compression to biaxial stretching. Combination of digital image correlation and experimental force vs. time evolutions allows determining the fracture strains and the instantaneous slope of the strain loading paths at the instant of cracking in principal strain space. Fractography using scanning electron microscopy helps identifying the crack opening modes corresponding to the different fracture strains. Results show that the proposed upset geometry sequence allows creating a new testing methodology for bulk forming similar to that of sheet forming with the widely used Nakajima test.

1. Introduction

The forming limit curve (FLC) defines the onset of necking in sheet metal forming and its determination by means of the Nakajima and Marciniak tests follows the international standard ISO-12004-2 [1]. In the case of the Nakajima test, at least five circular waisted geometries with different parallel shaft lengths must be employed to cover loading paths running from uniaxial tension to equal biaxial stretching in principal strain space.

The uncertainty in defining the onset of necking, the need to calibrate ductile damage at the onset of cracking, and the current practice of designing sheet metal parts based on thickness reduction rather than on necking, justifies the growing interest in the determination of the fracture forming limits (FFL). Fig. 1a illustrates how a Nakajima geometry sequence can be used to determine the theoretical fracture forming limit line with a slope of '−1′ corresponding to crack opening by tension (mode I) [2] in principal strain space.

The sharp changes in the strain loading paths towards plane strain deformation that occur after crossing the onset of necking (FLC) and the theoretical fracture forming limit line with a slope of '1′ corresponding to crack opening by in-plane shearing (mode II) [2] are also included in Fig. 1a.

Kobayashi [3] was among the first researchers to observe and analyze crack formation in bulk metal forming by upsetting cylindrical and ring test specimens with different aspect ratios, and various frictional conditions. Kuhn et al. [4] suggested the use of additional rolling and bending tests in specimens machined out from the same rods used for the cylindrical test specimens to obtain fracture strains under different loading paths. They described the FFL of bulk forming

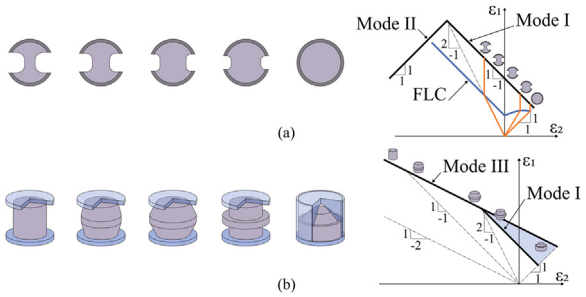

Fig. 1. Determination of the fracture forming limits (FFL) (a) in sheet metal forming using a Nakajima geometry sequence and (b) in bulk metal forming using various upset test geometries.

as a single line with slope '−1/2′ parallel to homogeneous (frictionless) uniaxial compression. This fracture limit line, not observed in sheet metal forming, is due to out-of-plane shearing (mode III), as it was later proved by Martins et al. [5] (Fig. 1b).

Erman et al. [6] proposed the utilization of tapered and flanged test specimens to obtain strain loading paths with small compressive strains and concluded that the FFL of bulk forming are bilinear due to combination of the above-mentioned line of slope '−1/2′ (mode III) with a line of slope '−1′ (mode I). Torsion and tensile tests were further suggested by Vujovic and Shabaik [7] to obtain loading paths with small compressive strains.

Suh et al. [8] made the first attempt to obtain fracture strains in the tension-tension quadrant of principal strain space by means of a flange-hub test specimen. The specimen failed by cracking under biaxial stretching with controlled frictional conditions but, in contrast to other geometries, it does not allow the observation of the instant

* Corresponding author.
E-mail address: pmartins@tecnico.ulisboa.pt (P.A.F. Martins).

https://doi.org/10.1016/j.cirp.2023.04.009

of fracture during upsetting because the region of interest is enclosed by the upper and lower dies.

In the above-mentioned investigations, and until the 2000's, the strain loading paths were experimentally determined by measuring the grid lines that were previously scribed (or etched) in the free surfaces of the specimens. The measurements were usually performed with toolmaker microscopes and required specimens to be removed from the tools at pre-determined amounts of deformation. The instant of fracture was generally determined by visual observation and, for this reason, often raised doubts in the fracture strain values.

In 1999, Kopp and Bernrath [9] proposed the use of acoustic emission analysis to determine the instant of cracking. They made use of the sudden release of energy emitted to the environment as sound pulses and combined acoustic emission with finite elements to determine the strain loading paths up to fracture of various upset test geometries like those pictured in Fig. 1b.

Although two decades separate the above-mentioned paper from the 2009 keynote paper by Volk et al. [10], a close reading of the latter allows concluding that the absence of international standards to determine the formability limits in bulk forming justifies the multiplicity of geometries and measurement procedures that have been proposed in the literature. In fact, it is surprising that no attempt has ever been made to create an upset geometry sequence capable of covering strain loading paths from homogeneous uniaxial compression to biaxial stretching in principal strain space. In other words, to create a bulk metal forming equivalent of the Nakajima geometry sequence that is widely used in the characterization of the formability limits by stretching in sheet metal forming.

In addition, it is worth noting that the first use of digital image correlation (DIC) to determine the strain loading paths up to fracture in bulk forming was only reported in 2018 [11].

Under these circumstances, this paper has a two-fold objective. Firstly, it proposes an original upset geometry sequence that can provide strain loading paths in both the tension-compression and the tension-tension quadrants of principal strain space. The sequence was inspired in a recent successful attempt of the authors to create an upset test geometry for obtaining the fracture strains in biaxial stretching [12].

Secondly, it presents an alternative analytical framework to that previously developed by the authors [12] to convert the experimental FFL and the corresponding region of uncertainty (light blue region in Fig. 1b) from principal strain space into the effective strain vs. stress triaxiality space. The framework accounts, for the first time ever, with the non-linear evolution of the strain loading paths obtained through DIC. Fractography using scanning electron microscopy (SEM) contributes to the characterization of the crack opening mechanisms.

2. Methods and procedures

2.1. Experimentation

Table 1 shows the new proposed upset geometry sequence for determining the FFL in bulk forming. A vertical cross-section is enclosed with a view of the main geometrical parameters: (i) the mid-height diameter D_o of the outer surface, (ii) the mid-height diameter D_i of the inner surface, (iii) the height H_o of the outer surface, (iv) the height H_i of the inner surface, (v) the center hole diameter d and (vi) the flat recess l of the outer surface.

Table 1
The new upset geometry sequence with dimensions in (mm).

Spec	UC	PSH	UT	PST	BS1	BS2	BS3
D_o	25	30	42	50	50	60	63
D_i	0	0	7.5	33.5	35	45	48
d	0	0	7.5	30	30	35	35
H_o	25	30	30	40	40	40	35
H_i	25	30	30	18	18	20	17
l	12.5	13.1	7.5	0	1	2	2
RP	1	1	1.43	5.06	5.67	7	7.4

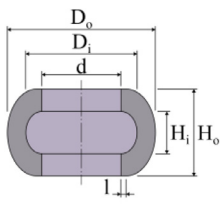

UC – Uniaxial compression
PSH – Pure shear
UT – Uniaxial tension
PST – Plane strain
BS – Biaxial stretching

The geometry sequence is based on the progressive evolution of a cylinder towards a thick-walled convex ring and is controlled by three design ratios: (i) ring proportion ratio $RP = 2D_m/(D_o - D_i)$, (ii) lateral slenderness ratio $LS = 2D_m/H_m$ and (iii) axial slenderness ratio $AS = H_m/(D_o - D_i)$, with an average diameter $D_m = (D_o + D_i)/2$ and an average height $H_m = (H_o + H_i)/2$.

The RP ratio, which is equal to $LS \times AS$, is a hollowness measure that quantifies the difference between a specific thick-walled ring and a cylinder. RP values increase from the leftmost specimen (a cylinder with RP=1) to the rightmost specimen of Table 1.

The LS and AS ratios control the outer mid-height diameter response to moments and forces. Their values also rise from the leftmost specimen (where $LS = 1$ and $AS = 1$) to the rightmost specimen with the objective of increasing convexity and eccentricity (LS), increasing axial slenderness (AS) and reducing the area moment of inertia.

The experiments were performed on aluminum AA7075-T6 supplied in the form of 200 mm diameter rods. The flow curve at ambient temperature (Fig. 2) was previously obtained by the authors by means of compression tests [12].

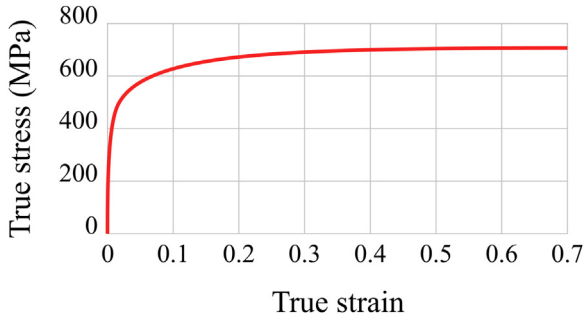

Fig. 2. Flow curve of the aluminum AA7075-T6.

The experimental evolutions of the major and minor strains with time were determined by DIC using a Dantec Dynamics Q-400 3D system equipped with two cameras of 6-megapixels resolution having 50.2 focal lenses and f/8 aperture (Fig. 3a). The specimens were painted in white and subsequently sprayed with a stochastic black dot pattern covering approximately 40% of their outer surfaces. They were illuminated with a spotlight during testing and the images were recorded with a frequency of 10 Hz having each black dot within a square of 8 × 8 pixels.

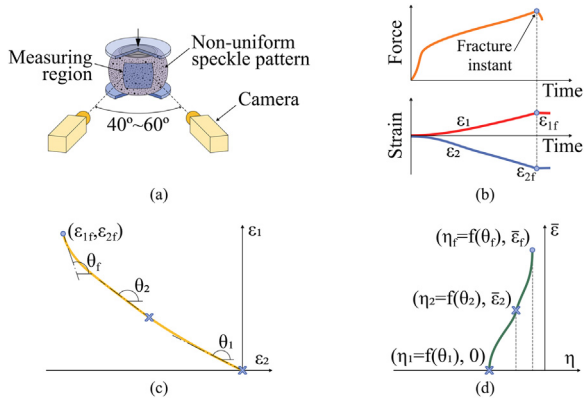

Fig. 3. Methodology for obtaining the experimental strain loading paths and the fracture instants: (a) Setup utilized in DIC, (b) combination of DIC with force vs. time evolution, (c) strain loading path and fracture strains in principal strain space and (d) fracture instant in the effective strain vs. stress-triaxiality space $\bar{\varepsilon} = f(\eta)$.

The instant of fracture was determined by merging the results of DIC with the evolution of the upsetting force with time (Fig. 3b) because crack opening is characterized by a sudden drop in force. The strain loading paths $\varepsilon_1 = f(\varepsilon_2)$ in principal strain space (Fig. 3c)

were obtained by elimination of time from the DIC evolutions of the major ε_1 and minor ε_2 strains.

The FFL in the effective strain vs. stress-triaxiality space $\bar{\varepsilon} = f(\eta)$, where $\eta = \sigma_m/\bar{\sigma}$ (Fig. 3d), were determined by analytical transformation of the entire set of experimental fracture strains $(\varepsilon_{1f},\ \varepsilon_{2f})$. The method considers the instantaneous slope $d\varepsilon_1/d\varepsilon_2 = \tan\theta_f$ of the strain loading paths at the instant of fracture (Fig. 3c) instead of assuming linear strain loading paths from beginning to the end, as it was previously done in [12].

2.2. Numerical simulation

Numerical simulation of the upset geometry sequence was carried out with the in-house finite element computer program i-form [13]. Material isotropy and rotational symmetric plastic deformation were assumed so that specimen cross-sections could be discretized by means of axisymmetric quadrilateral elements. The upper and lower compression plates were assumed to be rigid objects and discretized by linear contact-friction elements (Fig. 4). A friction factor $m = 0.1$ was used after checking the numerically predicted force vs. displacement evolutions that best matched the experimental ones.

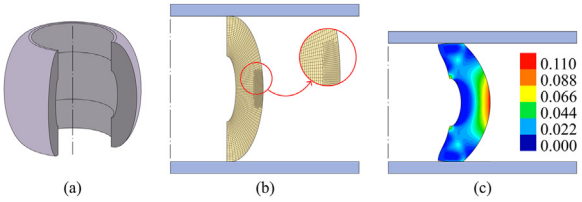

Fig. 4. (a) Drawing of the BS1 specimen (Table 1) with a section view, (b) initial finite element mesh with a detail and (c) final computed geometry with distribution of ductile damage (1).

The instant of fracture was modelled by means of a ductile damage criterion for bulk metal forming built upon combination of the Cockcroft-Latham (mode III) and McClintock (mode I) criteria,

$$D^{crit} = \int_0^{\bar{\varepsilon}_f} \frac{\sigma_1}{\bar{\sigma}} d\bar{\varepsilon} + C \int_0^{\bar{\varepsilon}_f} \left\langle \eta - \frac{1}{3} \right\rangle^2 d\bar{\varepsilon} \tag{1}$$

Fig. 4c shows the distribution of ductile damage at the instant immediately before fracture for the BS1 test specimen. As recently proved by the authors [12], the criterion (1) can easily model the uncertainty crack opening region of bulk metal forming resulting from the bilinear nature of the FFL for stress triaxiality values $\eta > 1/3$, which was firstly reported by Erman et al. [6].

3. Results and discussion

3.1. Fracture forming limits

Fig. 5 shows the experimental strain loading paths and the corresponding fracture strains for the entire set of test specimens listed in Table 1. Results were obtained in accordance with the methods and procedures that were previously described in Section 2.1 and show that the proposed upset geometry sequence covers strain loading paths running from uniaxial compression (UC) in the tension-compression quadrant to biaxial stretching (BS1-3) in the tension-tension quadrant, as the geometry evolves from a cylinder towards the slenderest thick-walled convex ring.

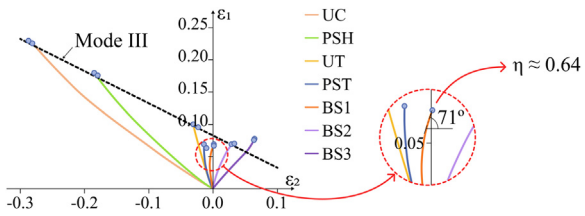

Fig. 5. Strain loading paths and fracture strains for the upset geometry sequence in principal strain space with a detail of the instantaneous slope at the instant of fracture for one of the test specimens.

The analytical framework to convert the fracture strains $(\varepsilon_{1f},\ \varepsilon_{2f})$ from principal strain space to the effective strain vs. stress triaxiality space, assumes material to be isotropic and cracks to be triggered on the outer (free) surface of the specimens under plane stress conditions $(\sigma_3 = 0)$. Then, by application of the Levy-Mises constitutive equations,

$$d\varepsilon_1 = \frac{d\bar{\varepsilon}}{\bar{\sigma}}\left(\sigma_1 - \frac{1}{2}\sigma_2\right) d\varepsilon_2 = \frac{d\bar{\varepsilon}}{\bar{\sigma}}\left(\sigma_2 - \frac{1}{2}\sigma_1\right) \tag{2}$$

and following Martins et al. [5], one can write the normalized principal stress $\sigma_1/\bar{\sigma}$ and the stress triaxiality η as a function of the ratio $\beta = d\varepsilon_2/d\varepsilon_1$ of the minor and major strain increments,

$$\frac{\sigma_1}{\bar{\sigma}} = \frac{(2+\beta)}{\sqrt{3}\sqrt{1+\beta+\beta^2}} \qquad \eta = \frac{(1+\beta)}{\sqrt{3}\sqrt{(1+\beta+\beta^2)}} \tag{3}$$

Now, considering the relationship $\beta = 1/\tan\theta_f$ at the instant of fracture and the ductile fracture criterion given by (1), it is possible to obtain the following expression for converting the fracture strains $(\varepsilon_{1f},\ \varepsilon_{2f})$ into the FFL in the effective strain vs. stress triaxiality space,

$$\bar{\varepsilon}_f = \frac{D^{crit}}{\frac{\sigma_1}{\bar{\sigma}} + C\left(\eta - \frac{1}{3}\right)^2} \qquad \frac{\sigma_1}{\bar{\sigma}} = f\langle tan\ \theta_f\rangle, \qquad \eta = g\langle tan\ \theta_f\rangle \tag{4}$$

The normalized principal stress $\sigma_1/\bar{\sigma}$ and the stress triaxiality η in (4) are determined from (3) using the experimental measurements of the instantaneous slope $d\varepsilon_1/d\varepsilon_2 = \tan\theta_f$ of the strain loading path at the instant of fracture for each specimen, as shown in Section 2.1 (Fig. 3).

The values of D^{crit} and C were obtained from experiments by means of a two-stage calibration procedure. The first parameter $D^{crit} = 0.11$, responsible for vertical translation of the FFL, was determined from specimens UC, PSH, and UT. The second parameter $C = \pm 3.9$, quantifying the influence of stress triaxiality and size of the 'uncertainty region' $(1/3 < \eta < 2/3)$ bounded by the two solid lines in the rightmost region of the FFL, was obtained from the PST, BS1, BS2, and BS3 specimens.

Application of the above-mentioned procedure for the fracture strains associated with the upset geometry sequence of Table 1 allows plotting the FFL given by (1) in the effective strain vs. stress triaxiality space, as it is shown in Fig. 6.

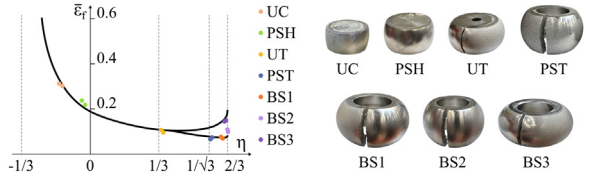

Fig. 6. Fracture forming limits derived from the upset geometry sequence in the effective strain vs. stress triaxiality space.

3.2. Crack opening modes

Figs. 7a to 7c show the finite element predicted distributions of ductile damage D and stress triaxiality η at the instant of fracture for the specimens labelled as PSH (pure shear), UT (uniaxial tension) and BS1 (biaxial stretching) in Table 1. Observation of the results at the mid-height position of the outer surfaces, allows concluding that stress triaxiality grows from $\eta \approx 0$ (PSH) to $\eta \approx 0.33$ (UT) and to $\eta \approx 0.61$ (BS1), as the geometry evolves towards the slender thick-walled convex ring.

The values of critical damage D^{crit} on the mid-height diameter of the specimen's outer surfaces are in good agreement with the location where cracks were triggered for each experimental case.

The SEM observations included in Figs. 7a to 7c are representative of the fracture surfaces of each specimen. As seen in Fig. 7a, the specimen with $\eta \approx 0$ (PSH) reveals a smooth fracture surface that is

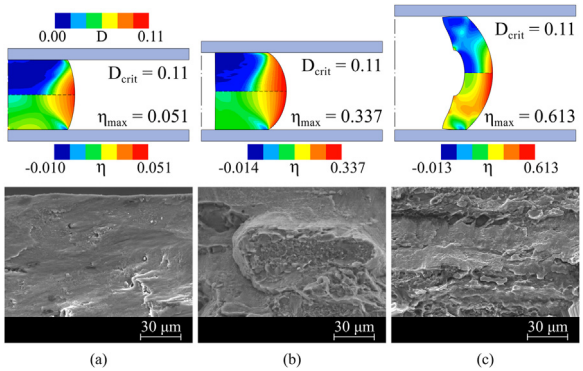

Fig. 7. Finite element computed distribution of ductile damage D according to (1) (top), and stress triaxiality η (bottom), plus SEM of the fracture surfaces for the test specimens (a) PSH, (b) UT, and (c) BS1.

consistent with crack opening by out-of-plane shear (mode III). The specimen with $\eta \approx 0.33$ (UT) discloses a predominant smooth fracture surface (Fig. 7b) typical of crack opening by mode III with some dimple structures that resemble those of crack opening by tension (mode I). Finally, the specimen with $\eta \approx 0.61$ (BS1) reveals a dimple-dominated structure (Fig. 7c) typical of mode I with neighboring smooth regions that are characteristic of mode III.

The results obtained for the UT and BS1 specimens of Table 1 cope with the existence of an uncertainty crack opening region for stress triaxiality values $\eta \geq 0.33$. Specimens with stress triaxiality values within this region of the FFL will generally give rise to crack opening by mixed modes I and III, which can be tension-dominant or shear-dominant, depending on the location of the fracture point inside the shadowed area of the FFL (refer to Fig. 1b).

3.3. Specimen design guidelines

After demonstrating the effectiveness of the proposed upset geometry sequence to cover a wide spectrum of strain loading paths and stress triaxiality values, it is important to provide guidance on the selection and design of the specimens. In practical terms, this is done by means of the specimen selection chart included in Fig. 8, which allows users to select the dimensionless geometry of their specimens (given by *RP*, *LS* and *AS* ratios) for specific required levels of stress triaxiality η at the mid-height diameter of the outer surfaces where fracture occurs.

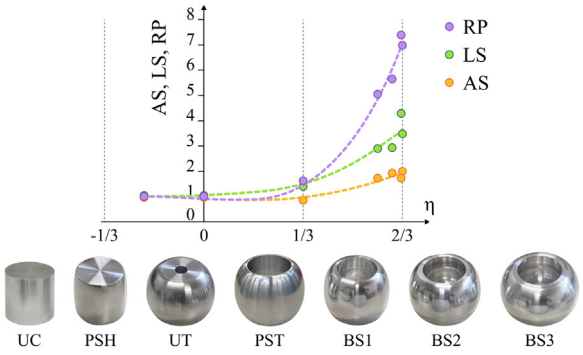

Fig. 8. Specimen selection chart with photographs of the upset geometry sequence used in the experiments.

The solid markers in Fig. 8 correspond to values of the ring proportion *RP*, lateral slenderness *LS* and axial slenderness *AS* ratios as a function of stress triaxiality η (at the instant of fracture) for the various test specimens used in this work. The solid lines result from fitting these values with trend lines and reveal that progression from uniaxial compression to biaxial stretching requires a strong increase in hollowness (*RP*) combined with significant increases in both lateral (*LS*) and axial (*AS*) slenderness. The increase in *LS* and *AS* result in the reduction of the area moment of inertia. This facilitates bending at the mid-height diameter of the outer surface, which in turn permits attaining biaxial stretching conditions (for increasing values of η) during upsetting.

The oscillation of values around the trend lines is due to minor adjustments that were made in selected test geometries after the need to scale down some of the specimens to cope with the maximum compressive force of the testing machine.

4. Conclusions

The new proposed upset geometry sequence provides fracture strains in a wide range of stress triaxiality values ranging from uniaxial compression to equal biaxial stretching. A new analytical procedure for converting these strains from principal strain space into the effective strain vs. stress-triaxiality space allows determining the FFL and the uncertainty region in which cracks open by tension and by out-of-plane shearing (mixed modes I and III). A specimen selection chart that relates three dimensionless geometry ratios with the required stress triaxiality values at the instant of fracture is provided for the choice and design of potential test specimen candidates.

Declaration of Competing Interest

The authors declare that they have no known competing financial interests or personal relationships that could have appeared to influence the work reported in this paper.

Acknowledgements

The support of Fundação para a Ciência e a Tecnologia of Portugal and IDMEC under LAETA-UIDB/50022/2020 and PTDC/EME-EME/0949/2020 is greatly acknowledged.

References

[1] ISO 12004-2. *Metallic Materials - Determination of Forming-Limit Curves for Sheet and Strip - Part 2: Determination of Forming-Limit Curves in the Laboratory*, International Organization for StandardizationGeneva, Switzerland.
[2] Isik K, Silva MB, Tekkaya AE, Martins PAF (2014) Formability Limits by Fracture in Sheet Metal Forming. *Journal of Materials Processing Technology* 214:1557–1565.
[3] Kobayashi S (1970) Deformation Characteristics and Ductile Fracture of 1040 Steel in Simple Upsetting of Solid Cylinders and Rings. *Journal of Engineering for Industry* 92:391–398.
[4] Kuhn HA, Lee PW, Erturk A (1973) A Fracture Criterion for Cold Forging. *Journal of Engineering Materials and Technology* 95:218–231.
[5] Martins PAF, Bay N, Tekkaya AE, Atkins AG (2014) Characterization of Fracture Loci in Metal Forming. *International Journal of Mechanical Sciences* 83:112–123.
[6] Erman E, Kuhn HA, Fitzsimons G (1983) Novel Test Specimens for Workability Testing. in Chait R, Papirno R, (Eds.) *Compression Testing of Homogeneous Materials and Composites*, ASTM International, West Conshohocken, 279–290.
[7] Vujovic V, Shabaik AH (1986) A New Workability Criterion for Ductile Metals. *Journal of Engineering Materials and Technology* 108:245–249.
[8] Suh SK, Kuhn HA, Downey CL (1976) Metal Flow and Fracture in an Extrusion-Forging Process. *Journal of Materials Processing Technology* 98:330–336.
[9] Kopp R, Bernrath G (1999) The Determination of Formability for Cold and Hot Forming Conditions. *Steel Research* 70:147–153.
[10] Volk W, Groche P, Brosius P, Ghiotti A, Kinsey BL, Liewald M, Madej L, Min J, Yanagimoto J (2019) Models and Modelling for Process Limits in Metal Forming. *CIRP Annals - Manufacturing Technology* 68:775–798.
[11] Magrinho JP, Silva MB, Alves LM, Atkins AG, Martins PAF (2018) New Methodology for the Characterization of Failure by Fracture in Bulk Forming. *Journal of Strain Analysis* 53:242–247.
[12] Sampaio RFV, Pragana JPM, Bragança IMF, Silva CMA, Martins PAF (2022) Revisiting the Fracture Forming Limits of Bulk Forming Under Biaxial Tension. *International Journal of Damage Mechanics* 31:882–900.
[13] Nielsen CV, Martins PAF (2021) *Metal Forming: Formability, Simulation, and Tool Design*, Academic PressNew York, USA.